RSC Advances

PAPER

View Article Online
View Journal | View Issue

Cite this: *RSC Adv.*, 2026, **16**, 20999

Activated charcoal modified Ag and Cu-anatase TiO_2 for superior photocatalytic degradation of doxycycline under visible-solar light irradiation

Kirti Bisht, Davinder Kaur and Bonamali Pal *

Doxycycline, a frequently used tetracycline antibiotic, remains in the environment due to its widespread use, long-term biological stability, and toxicity even at low concentrations. In this regard, this paper addresses the synthesis, characterisation, and modification of anatase TiO_2 for doxycycline degradation under visible and solar light. The 2 wt% Ag and Cu–TiO_2 was prepared *via* a hydrothermal reaction followed by photodeposition. To improve the adsorption capacity, the composites underwent additional modification with activated charcoal *via* ultrasonication. Their physicochemical properties were analyzed using XRD, FE-SEM, HR-TEM, XPS, BET, PL, TRPL, and UV-DRS techniques. The results demonstrate that the incorporation of Ag and Cu and activated charcoal into anatase TiO_2 led to enhanced crystallinity, a mesoporous structure, improved light absorption, and an increased surface area. Among modified composites, the AC (1 wt%)–Cu (2 wt%)–TiO_2 composite showed the highest adsorption and photocatalytic activity, removing up to 98.5% of doxycycline under solar light and 88.8% under visible light. This outperformed AC (1 wt%)–Ag (2 wt%)–TiO_2 (92.6%) > Cu (2 wt%)–TiO_2 (89.2%) > Ag (2 wt%)–TiO_2 (83.9%) > AC (1 wt%)–TiO_2 (77.4%) > TiO_2 (68.7%). This improvement is due to the surface plasmon resonance (SPR) effect of Cu, increased electron mobility, and the larger surface area of activated charcoal. The catalyst demonstrates excellent stability and reusability. Furthermore, HR-MS analysis was used to identify the degradation pathways of doxycycline, complemented by TOC testing and the detection of active species. Due to its enhanced catalytic performance, affordability, and eco-friendliness, the reported composite is a promising option for pharmaceutical wastewater treatment.

Received 1st January 2026
Accepted 7th April 2026

DOI: 10.1039/d6ra00006a

rsc.li/rsc-advances

1 Introduction

The presence of pharmaceutical compounds in aquatic environments poses serious ecological and health concerns. Although antibiotics have been widely used for decades to treat infectious diseases in humans and animals, they often show poor absorption in biological systems. Consequently, these substances are frequently released into the environment through various pathways, including rainwater runoff, animal husbandry, hospital waste, municipal sewage, and composting processes.[1–3] Both human and veterinary medicines use the broad-spectrum antibiotic doxycycline (DOX). Its widespread application and environmental stability make it a significant contaminant. Even at low doses, doxycycline's antibacterial effects can lead to resistance in microorganisms, disrupt microbial communities and functions, and pose significant risks to humans and animals.[4] Recent studies have shown that DOX levels in wastewater and surface waters range from 0.1 to 460 μg L^{-1}.[5] As a result, developing efficient and environmentally friendly methods to remove doxycycline is essential for combating antibiotic contamination in aquatic environments.

The reported methods for removing DOX from water include advanced oxidation,[6] electrocoagulation,[7] adsorption,[8,9] biodegradation,[10] and photodegradation techniques.[11,12] Nevertheless, there are drawbacks, including the fact that antibiotics are less effective, difficult to remove, and contribute to secondary contamination. Using light instead of chemicals, photodegradation is an economical, efficient, and environmentally benign method of eliminating hazardous pollutants. Light exposure causes electron–hole pairs to form on the surface of the semiconductor photocatalyst, initiating redox reactions.[13] Semiconductors such as TiO_2 and ZnO can be utilized in photocatalysis for water splitting using solar energy, enabling the production of H_2 and other environmental applications.[14–16]

Among the most researched photocatalytic materials, TiO_2 is widely regarded as the most practical semiconductor photocatalyst due to its favourable physicochemical properties, including chemical inertness, a suitable band position, affordability, biocompatibility, photochemical activity, and non-toxicity.[17] However, its use is limited due to a significant band

Department of Chemistry and Biochemistry, Thapar Institute of Engineering and Technology, Patiala, Punjab 147004, India. E-mail: bpal@thapar.edu

gap that only enables activation by ultraviolet light, which accounts for roughly 5% of the sunlight. Moreover, fast recombination of photoinduced electron–hole pairs considerably decreases its photocatalytic efficacy.[18] Various modification techniques have been used to improve their optical absorption in the visible light range. Depositing noble metals on TiO_2 is common due to their advantageous properties, including biological affinity, easy reduction, surface plasmon resonance (SPR), and chemical stability.[19,20] The effective separation of photogenerated charges is facilitated by the Schottky barrier that forms at the metal-TiO_2 interface.[21,22]

Another factor influencing the photocatalytic effectiveness of the photocatalyst is its surface area. It has been shown that carbonaceous materials and TiO_2 composites significantly enhance the photocatalytic process, often utilizing activated charcoal, carbon nanotubes, graphene and its derivatives, and biochar.[23,24] Although activated charcoal (AC) lacks photocatalytic activity, it facilitates pollutants to get adsorbed onto its surface, which increases the photocatalytic interaction between TiO_2 and impurities.[25] This increased adsorption leads to a higher concentration of contaminants near the active sites of TiO_2. Activated charcoal is recognized as a stable, cost-effective, and environmentally friendly material, known for its well-developed pore structure, large surface area, and high adsorption capacity. The AC in the metal-TiO_2 catalyst facilitates the transfer of organic molecules to the degradation site, thereby enhancing the overall efficiency of the process.[26]

A comprehensive review of the literature indicates that substantial research has concentrated on the photoactivity of activated charcoal-loaded TiO_2, metal (Cu, Ag, Au, *etc.*)-TiO_2, and activated charcoal-loaded metal-TiO_2, as well as their efficiency in degrading organic pollutants. Girija *et al.* modified TiO_2 with activated charcoal and Fe (AC-Fe: TiO_2), which demonstrated 98% removal of Methylene blue under visible light.[27] Baruah *et al.* investigated the photocatalytic degradation of anthracene using Ni-doped TiO_2-activated charcoal (Ni–TiO_2@C) synthesized *via* a hydrothermal method. The degradation efficiency reaches 99.9% within 50 minutes under visible light.[28] Yaacob *et al.* synthesized AC/TiO_2–Cu ternary composite *via* a microwave-assisted sol–gel method, achieving 89% degradation of metronidazole under UV light.[29] Baruah *et al.* synthesized a Fe-doped TiO_2 activated carbon nanocomposite (FDT/PAC) and observed that 100% degradation was achieved for Congo red, *E. coli*, and *S. aureus* within 60 minutes, 120 minutes, and 75 minutes, respectively, under visible light irradiation.[30] However, reports on studies using activated charcoal-loaded Ag and Cu–TiO_2 for the efficient removal of doxycycline under visible and solar light are less explored.

The aim of this study is to study the influence of activated charcoal, Ag, and Cu on the photocatalytic activity of anatase TiO_2 for the removal of doxycycline under visible and solar light exposure. This study represents the synthesis of anatase-phase TiO_2, Ag and Cu–TiO_2, and activated charcoal-loaded Ag and Cu–TiO_2 composites using hydrothermal, photodeposition, and ultrasonication methods, respectively. The Ag and Cu NPs serve as co-catalysts to improve charge separation and increase light absorption, while activated charcoal is added to enhance the surface area and adsorption capacity of the photocatalysts. Additionally, the photocatalytic activity of the as-prepared catalysts for the breakdown of doxycycline under sunlight was investigated. The novelty and importance of this study are established by the fact that the degradation of doxycycline using activated charcoal-loaded Ag and Cu–TiO_2 has not been previously documented. This research advances the development of effective, eco-friendly, and low-cost composites for removing antibiotic pollutants from wastewater.

2 Materials and methods

2.1. Chemicals and materials

Titanium tetra-isopropoxide (TTIP) and silver nitrate ($AgNO_3$) were purchased from Sigma-Aldrich, India. Copper nitrate hexahydrate [$Cu(NO_3)_2 \cdot 6H_20$], sodium hydroxide (NaOH), and Isopropyl alcohol (IPA) were acquired from Loba Chemie, India. Ethanol was purchased from SD Fine Ltd. Triple-deionized (DI) water was supplied by Organo Biotech Laboratories Pvt. Ltd, India. Activated Charcoal (AC) was bought from Central Drug House (P) Ltd Doxycycline (DOX) drug tablets were purchased from a local drug store.

2.2. Synthesis of TiO_2 nanoparticles

Anatase TiO_2 nanoparticles were produced using a hydrothermal approach.[31] In a typical synthesis, 5 mL of TTIP was added to 100 mL deionized water and agitated for 3 hours to ensure complete dissolution. After that, a 0.5 mM sodium hydroxide (NaOH) solution was added dropwise, and the mixture was continuously stirred for 30 minutes. A white precipitate has been produced as a result of this gradual addition, and the pH of the solution has been kept at 7 to provide ideal precipitation conditions. After that, the mixture was sealed in a stainless-steel autoclave coated with Teflon and kept at 180 °C for 24 hours. Following centrifugation, the precipitates were collected, successively washed with ethanol and distilled water, and then dried for three hours at 80 °C. Following that, as illustrated in Scheme 1, the dried sample was annealed for five hours at 400 °C.

2.3. Synthesis of Ag and Cu–TiO_2

The photo-deposition technique was utilized to deposit a 2 wt% Ag and Cu catalyst onto TiO_2.[24] As depicted in Scheme 1, initially, 100 mg of powdered TiO_2 was dispersed in a 50% v/v aqueous IPA solution. After adding 1852 μL of 0.01 M $AgNO_3$ solution, the test tubes were purged with argon gas for 15 minutes after being sealed with a rubber septum. It was then exposed to UV light (a mercury arc lamp with an intensity of 125 W m^{-2}) for 2 hours while being constantly stirred. The suspension was washed successively with DI water and ethanol, followed by drying at 70 °C for 4–5 hours. The Ag (2 wt%)-TiO_2 sample obtained is abbreviated as A_2T. The same procedure was implemented for photo-deposition of 2wt% Cu, utilizing [$Cu(NO_3)_2 \cdot 6H_20$] (0.01 M, 3125 μL), and the sample obtained is abbreviated as Cu_2T.

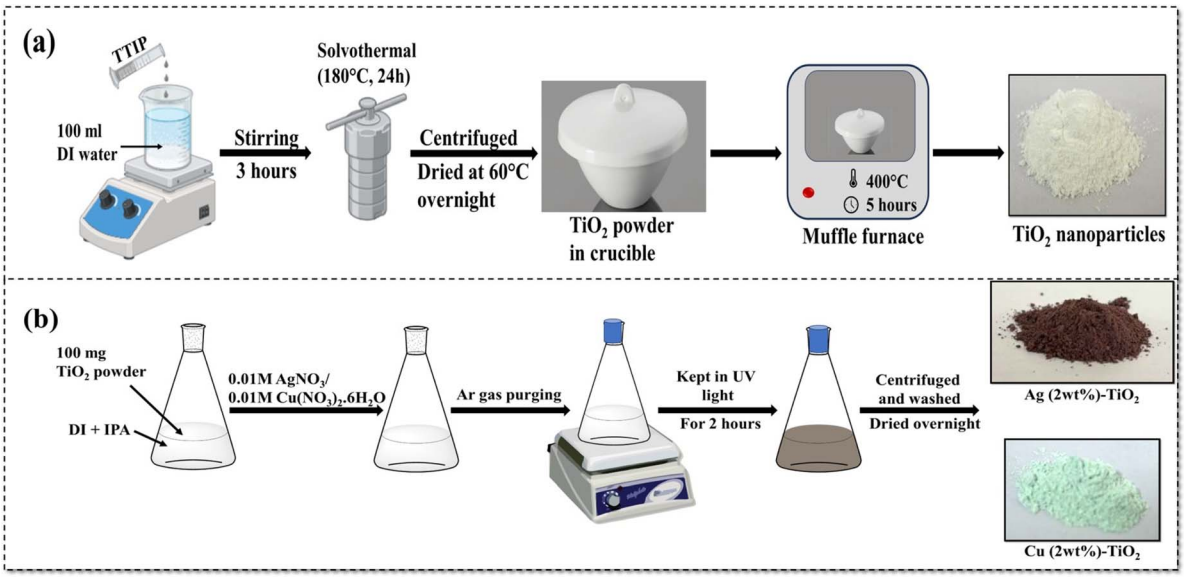

Scheme 1 Schematic representation of the procedure for synthesizing (a) anatase TiO_2, (b) Ag/Cu(2 wt%)–TiO_2.

2.4. Synthesis of AC–TiO_2 & AC modified Ag–TiO_2 and Cu–TiO_2

The activated charcoal-modified composites were produced using the ultrasonication method followed by the Calcination. 2 mg AC was distributed in 20 mL of ethanol and ultrasonicated for 1 hour. To the previous solution, add 200 mg TiO_2 powder (A_2T for AC–Ag–TiO_2 and Cu_2T for AC–Cu–TiO_2) and further sonicate for 1 hour. To ensure a homogeneous suspension, the resultant solution was magnetically stirred at room temperature for 24 hours. The composite was then washed several times with DI water and ethanol using centrifugation, dried overnight at 70 °C, and finally annealed at 500 °C for 2 hours. AC (1 wt%)–TiO_2, AC (1 wt%)–Ag (2 wt%)–TiO_2, and AC (1 wt%)–Cu (2 wt%)–TiO_2 are denoted as TC_1, A_2TC_1, and Cu_2TC_1, respectively.

2.5. Characterization techniques

X-ray diffraction analysis was used to identify the crystal phase of the photocatalysts in their initial state. The study employed a PANalytical X'pert PRO X-ray diffractometer, operated with Cu-Kα radiation at a wavelength of 1.54060 Å, with a scan range of 10° to 80° (2θ). Using FE-SEM (Carl-Zeiss SIGMA 500) and HR-TEM (JEOL, JEM 2100 PLUS) analysis, the morphological and structural features were investigated. The optical absorption spectra of every sample were examined using a UV-visible spectrophotometer (JASCO, V-750). The diffuse reflectance spectra were recorded in wavelength range of 200–800 nm, using barium sulphate ($BaSO_4$) as the reference standard. A SHIMADZU RF-6000 spectrofluorometer was used for the photoluminescence (PL) tests, which were carried out at room temperature and stimulated at 300 nm. A HORIBA DeltaFlex TCSPC Fluorescence Lifetime Spectrofluorometer was used for time-resolved studies. The change in UV-visible absorption spectra during the degradation of pollutants were analyzed with a JASCO V-750 spectrophotometer. The electronic states of the synthesized samples were examined using a Thermo Fisher Scientific X-ray photoelectron spectrometer (XPS) equipped with a Kα X-ray source. A Quantachrome Nova 1000 surface analyzer was used to quantify the surface area and pore diameter using the BET and BJH techniques. Following a wet oxidation procedure, TOC analysis using FAS (ferrous ammonium sulfate) titration. The QTOF mass spectrometer, coupled with UPLC and a PDA detector operating in the 190–800 nm range, was used to perform HRMS analysis for the identification of reaction by-products.

2.6. Photocatalytic activity studies

The photodegradation of the pharmaceutical drug, doxycycline (DOX), under the influence of solar light irradiation and LED visible light was assessed using the photoactivity of bare anatase TiO_2 and several modified composites. The setup of photodegradation experiment is given in Fig. S1. Dark adsorption and photolysis studies were carried out prior to the degradation experiment. Usually, 5 mg of catalyst was uniformly added to each test tube with 10 mL of a 50 ppm DOX solution. The reaction mixture was held in the dark for 30 minutes before irradiation to establish an adsorption–desorption equilibrium. Following that, a 50 W LED lamp (with intensity ~100 W m^{-2}) was turned on to observe photodegradation over different time intervals. The catalyst was periodically removed from the solutions *via* centrifugation to remove any residual solid particles. The supernate was then analyzed with a UV-Visible spectrophotometer. By examining fluctuations in the principal absorption peak of DOX at $\lambda_{max} = 345$ nm across different time periods, changes in the DOX concentration were monitored. The following formula was used to obtain the percent effectiveness (%) of photocatalytic drug degradation:

$$\eta(\%) = \frac{C_0 - C_t}{C_0} \times 100 \quad (1)$$

Here, η represents the photocatalytic efficacy, C_0 and C_t denote the initial concentration of DOX and the concentration after 't' minutes of exposure to visible light, respectively.

3 Results and discussion

3.1. Crystallographic, structural, and surface morphological studies

The crystal planes and corresponding diffraction angle values for the synthesized composites were thoroughly analyzed along with bare activated carbon, as presented in Fig. 1(a). Activated charcoal exhibits broad peaks from 20° to 30° and 40° to 48° in 2θ values, corresponding to the (002) and (100) planes (shown in Fig. S2), indicating a primarily amorphous structure, which is characteristic of it. The diffraction peaks observed at 2θ values of 25.3, 37.8, 48.1, 53.9, 55.1, 62.8, 68.7, 70.8, and 75.1 indicate the formation of the anatase phase TiO_2, corresponding to the (101), (004), (200), (105), (211), (204), (116), (220), and (215) crystal planes. The results obtained are in strong alignment with JCPDS Card No. 21-1272.[31] The distinct and sharp diffraction peaks clearly demonstrate that the synthesized TiO_2 exhibits a high degree of crystallinity and a well-organized structural framework, confirming the quality of the material. We did not find any secondary peaks associated with other phases in the pure sample, indicating that the formed TiO_2 consists solely of the anatase phase. After photo-deposition of Ag and Cu metals onto TiO_2, no distinguishable peaks for Ag and Cu co-catalysts were identified. According to earlier research, metal nanoparticles with a low weight percentage (less than 5 wt%) cannot be identified by XRD spectra.[32] When AC was added, the AC-related diffraction peak decreased significantly, almost disappearing. This result suggests that doping with AC has no noticeable effect on the lattice structure of TiO_2, and that the crystallinity of TiO_2 in the anatase phase remains constant. This lack of influence can be ascribed to the higher X-ray scattering coefficients of Ag, Cu, and TiO_2 relative to AC, owing to their greater atomic numbers.

The FTIR analysis, shown in Fig. 1(b), is used to examine the surface functional groups of bare anatase TiO_2 and the various prepared composites. The broad absorption band around 3000-3400 cm^{-1} results from the fundamental O–H stretch of the hydroxyl group, which may serve as a pollutant concentrator and facilitate the diffusion between the target pollutant and TiO_2 surface.[33] The weak band at 1630 cm^{-1} indicates O–H bending from chemically adsorbed water molecules.[34] The peaks appeared in the lower fingerprint region (below 800 cm^{-1}) are assigned to translational modes of metal–oxygen– metal (Ti–O–Ti) and metal–oxygen (Ti–O) linkages.[35] A new peak appears in A_2TC_1 and Cu_2TC_1 composites at approximately 1050-1150 cm^{-1}, corresponding to Ti–O stretching. This indicates surface conjugations *via* oxygen atoms between the bulk activated carbons and the Ti–O groups bonds.[36]

The morphology of the as-prepared nanocomposites was assessed using FE-SEM. From Fig. 2, it can be seen that all synthesized heterostructures exhibit a spherical-like morphology, similar to that of the synthesized anatase TiO_2. The uneven distribution of activated charcoal over TiO_2 nanoparticles is shown in Fig. 2(b). The low weight% deposition of Ag and Cu, respectively, on the TiO_2 surface of the A_2T and Cu_2T composites was not detectable, as shown in Fig. 2(c and e). The EDS technique was employed to determine the elemental composition of the sample and to quantify its relative abundance. In Fig. 2(d and f), EDS confirms the presence of Ag in the A_2T and Cu in Cu_2T composites. The elemental composition of Ag in A_2T and Cu in Cu_2T was found to be 1.26 wt% and 1.34 wt%, respectively, which closely align with the 2 wt% of Ag and Cu photo-deposited over TiO_2. The disparity between the anticipated and actual elemental weight percentages is caused by the restricted scanning area of a given catalyst location, as well as inevitable loss during the washing process. Fig. S3 depicts FE-SEM images of A_2TC_1 and Cu_2TC_1 composites.

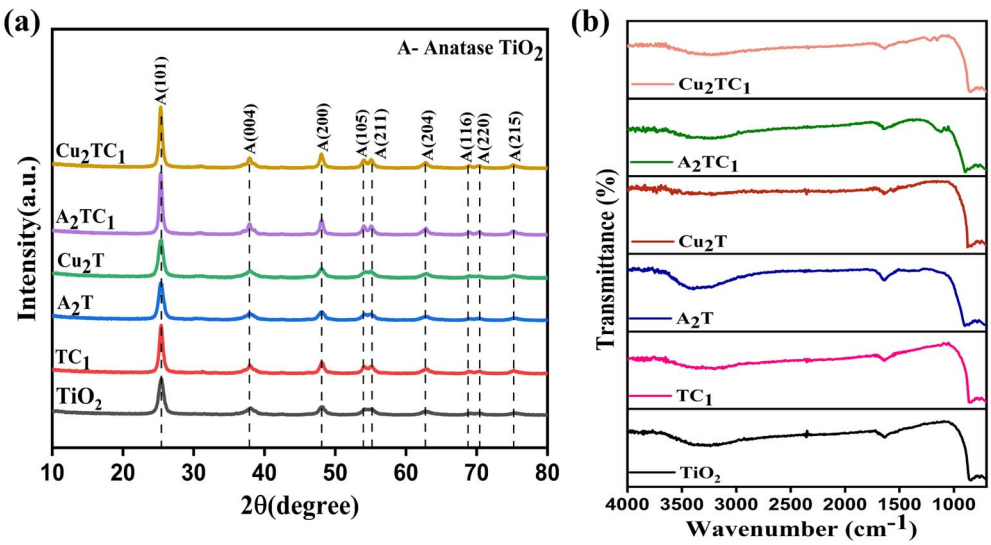

Fig. 1 (a) X-ray diffraction patterns and (b) FTIR spectra of the anatase TiO_2 and its modified composites.

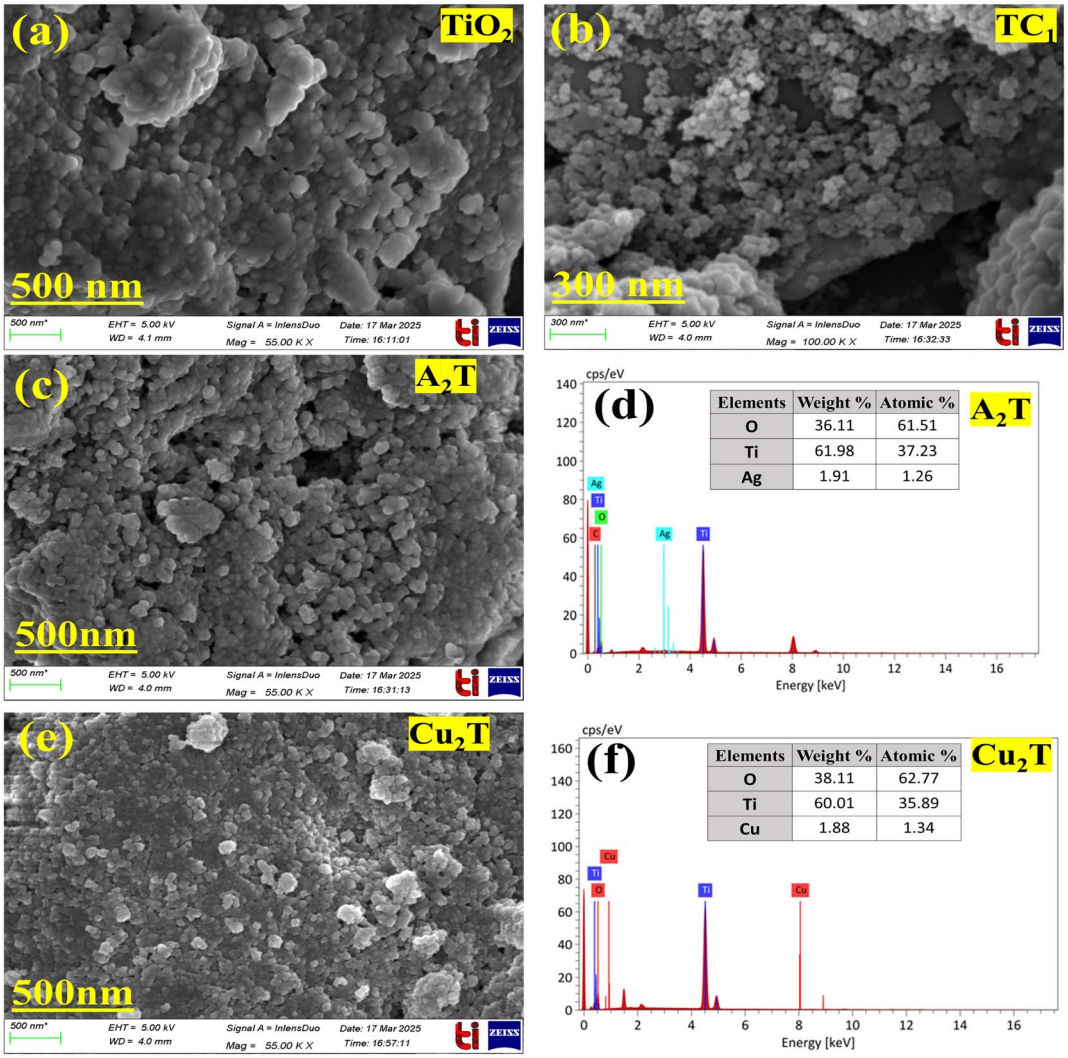

Fig. 2 FE-SEM image of (a) anatase TiO_2, (b) AC (1 wt%)–TiO_2, FE-SEM images and EDS spectra of (c and d) Ag (2 wt%)–TiO_2, (e and f) Cu (2 wt%)–TiO_2.

Additionally, HR-TEM analysis was performed for A_2T, Cu_2T, and Cu_2TC_1 (Fig. 3) composites. HR-TEM micrographs of Ag and Cu-deposited TiO_2 obtained at different magnifications reveal small black dots that indicate the presence of Ag and Cu over TiO_2, as depicted in Fig. 3(a–d). The existence of the metallic Cu (111) diffraction plane is clearly visible in Fig. 3(e–f) of the Cu_2TC_1 composite. This is explained by a lattice fringe with a *d*-spacing of 0.217 nm, whereas a lattice fringe with a *d*-spacing of 0.393 nm characterizes the (101) crystal plane of TiO_2. The corresponding selected-area electron diffraction (SAED) patterns of A_2T, Cu_2T, and Cu_2TC_1, showing intense spot and ring patterns, are shown in Fig. 3(c, f and i), respectively. For each ring pattern, the *d*-spacing has been calculated, and the corresponding planes have been identified and marked in the figure.

3.2. Surface area and porosity analysis

The surface characteristics and pore size distributions of the synthesized material were examined through analysis of the N_2 adsorption–desorption isotherms, as illustrated in Fig. 4. A type IV isotherm with a noticeable H3 hysteresis loop was seen in both the bare TiO_2 and the generated Cu_2TC_1 composite, indicating multilayer adsorption and confirming a mesoporous structure. The inset table in Fig. 4 provides detailed information on the pore structure parameters and surface area. The surface area for bare TiO_2, as determined by the BET method, was found to be 52.2 $m^2\ g^{-1}$, which increased to 55.6 $m^2\ g^{-1}$ with the addition of AC and Cu to the TiO_2.

The pore diameter and volume were obtained using the Barrett–Joyner–Halenda (BJH) model. Both Cu_2TC_1 and bare TiO_2 have computed pore diameters of 14.6 nm and 15.08 nm, respectively, and pore volumes of 0.242 cc g^{-1} and 0.226 cc g^{-1}, respectively. The presence of Cu and AC occupying the pores of TiO_2 may be the cause of the observed decrease in pore diameter.

3.3. Optical studies

A photoluminescence spectrum technique was used to evaluate the transfer mechanisms, excitation, and recombination rates

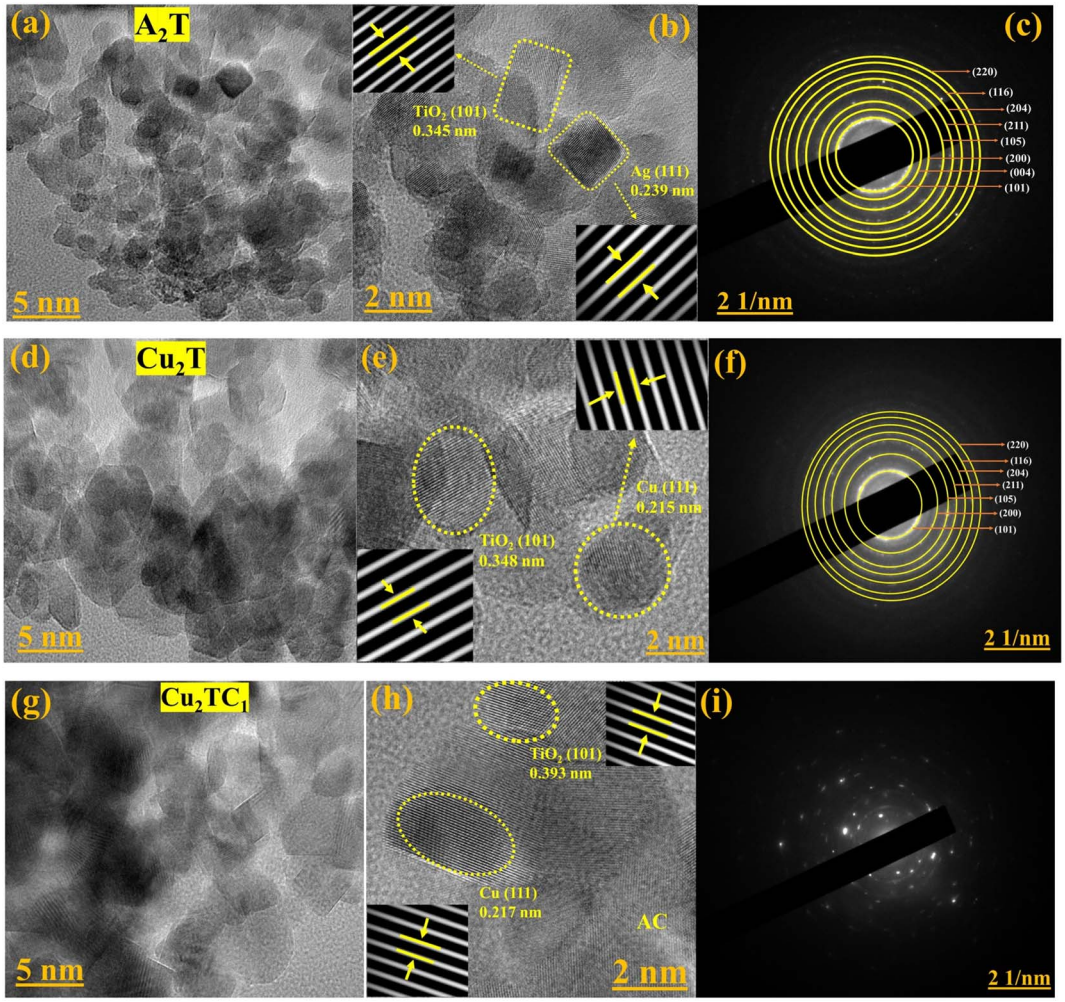

Fig. 3 HR-TEM images and SAED pattern of (a–c) Ag (2 wt%)–TiO_2, (d–f) Cu (2 wt%)–TiO_2, (g–i) AC (1 wt%)–Cu (2 wt%)–TiO_2 composites.

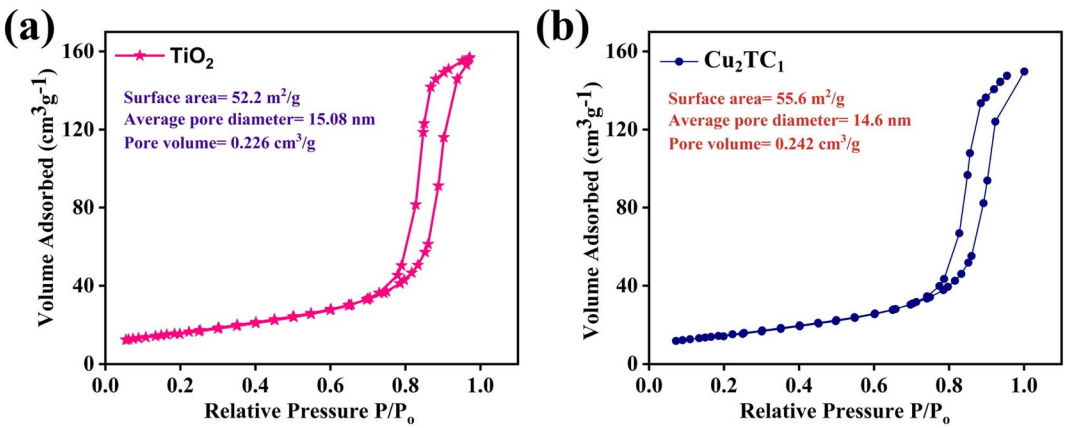

Fig. 4 BET adsorption isotherm of (a) anatase TiO_2, (b) AC (1 wt%)–Cu (2 wt%)–TiO_2.

of electron–hole pairs at λ_{max} = 300 nm. A decrease in PL intensity is frequently a sign of a longer lifetime of photoexcited electron–hole pairs.[37–39] When compared to bare TiO_2, the composites with Ag and Cu (2 wt%) showed reduced intensity (Fig. 5). Likewise, the AC-loaded composites showed less intensity than TC_1, suggesting that the A_2TC_1 and Cu_2TC_1 composites have higher charge transfer efficiency than TC_1. The increased electrical conductivity brought about by AC and the

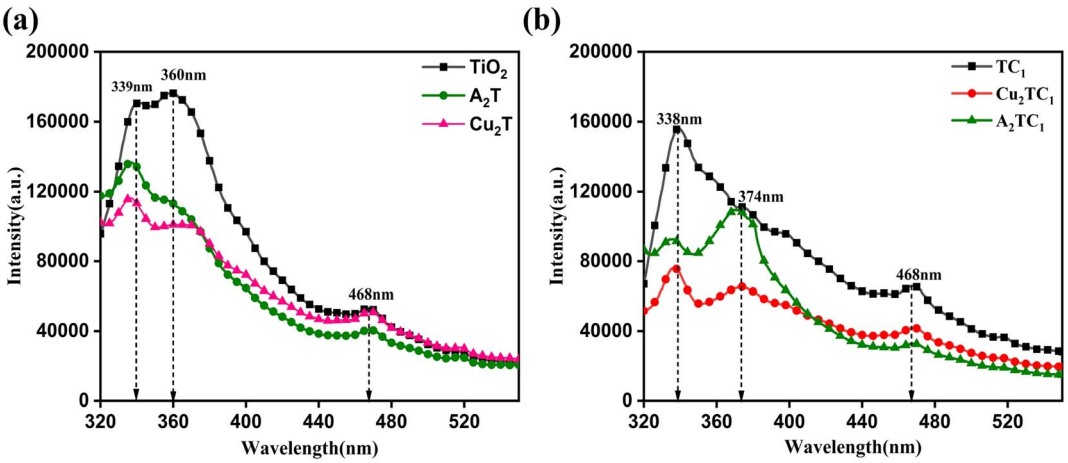

Fig. 5 Photoluminescence spectra of (a) TiO_2, A_2T, Cu_2T, (b) TC_1, Cu_2TC_1, A_2TC_1composites.

SPR effect brought on by the addition of Ag and Cu NPs may be responsible for the decrease in PL signal intensity. These findings are reinforced by experimental Time-Resolved Photoluminescence (TRPL) analysis (Fig. S4 and Table S1), showing that Cu_2TC_1 has a longer average lifetime (0.735 ns) compared to Cu_2T (0.205 ns) and Bare TiO_2 (0.153 ns). This extended lifetime indicates effective charge transfer and reduced recombination of the photoexcited electron–hole pair.

The quantum yield (ϕ) of the composites was calculated with the following equation using quinine sulfate[40] as a reference ($\phi_R = 0.546$)

$$\phi = \phi_R \times \frac{I_s}{I_R} \times \frac{A_R}{A_s} \times \frac{{\eta_s}^2}{{\eta_R}^2} \quad (2)$$

where A and I represent absorbance and area under the fluorescence emission, respectively. η is the refractive index of the solvent. The subscripts S and R denote sample and reference, respectively. The quantum yield of the composites ($A_2TC_1 = 0.240$ and $Cu_2TC_1 = 0.210$) calculated using eqn (2) is found to be lower than that of the bare TiO_2 (0.316) due to the decrease in the integrated area under the PL emission curve.

Fig. 6(a) shows the UV-vis diffuse reflectance spectra of various modified composites and anatase TiO_2. Significant absorbance of the bare TiO_2 is visible in the UV spectrum, with a peak absorption at about 350 nm. The observed absorbance in TiO_2 is due to electrons moving to the conduction band (CB) 3d orbital of Ti from the valence band (VB) 2p orbital of O.[41,42] In the case of Cu-deposited composites (Cu_2T and Cu_2TC_1), the absorption edge shifts towards longer wavelength (600-800 nm), showing a red shift in the TiO_2 absorption band, whereas the Ag-deposited composites (A_2T and A_2TC_1) display a broad band at 400–600 nm.

These absorption bands are attributed to the plasmonic bands of noble metals Ag and Cu, which enable the visible light activation of UV-responsive TiO_2. When Ag and Cu and AC are both added to TiO_2, the resulting hybrid exhibits a significantly broader absorption band across the visible spectrum and an increased light absorption intensity.

The DRS spectra were analyzed using the Kubelka–Munk equation, as presented in eqn (3). The linear portion of the curve in Tauc's figure (αhv *vs.* hv) was extended to the x-axis in order to get the bandgap energy of the composites.

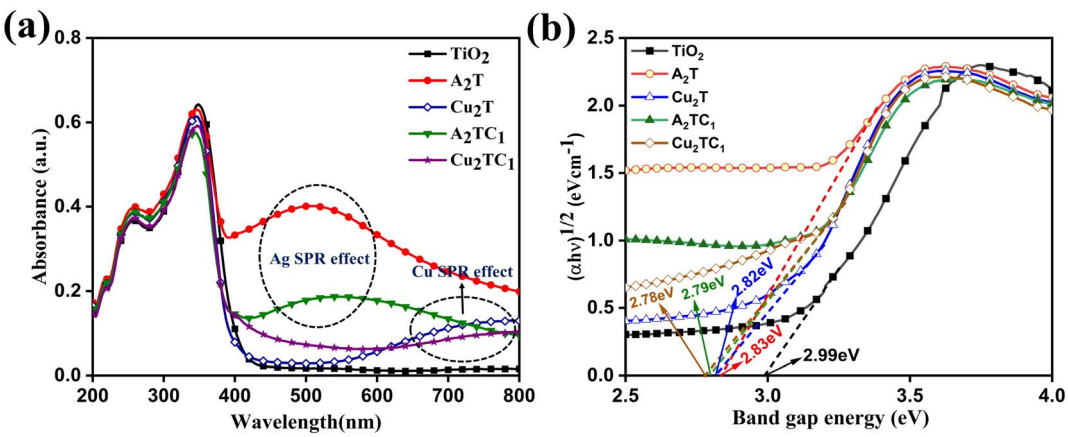

Fig. 6 (a) Diffuse reflectance spectra and (b) Tauc plots for allowed direct transition of the as-prepared composites.

$$\alpha h\nu = A(h\nu - E_g)^n \quad (3)$$

where ν is the light frequency, h is Planck's constant, and α is the absorption coefficient. E_g is the bandgap energy, while A is a constant. The numbers $\frac{1}{2}$ and 2 denotes allowed direct and indirect electronic transitions for the variable n, respectively. Fig. 6(b) illustrates that the ternary composite Cu_2TC_1 possesses the narrowest bandgap energy (2.78 eV) as compared to bare anatase TiO_2 (2.99 eV), A_2T (2.83 eV), Cu_2T (2.82 eV), and A_2TC_1 (2.79 eV). As a result of the reduced band gap, the ternary Cu_2TC_1 composite will require less energy to transfer electrons from the VB to the CB. The impact of Cu and AC in lowering the bandgap and enhancing the optical characteristics of TiO_2 composites in the visible spectrum is highlighted by this drop in bandgap values.

3.4. XPS analysis

XPS analysis was conducted to ascertain the chemical states, core-level binding energies, and elemental composition of the constituent elements. The survey spectrum and the deconvoluted spectrum of A_2TC_1 composite are given in Fig. S5. The survey spectrum of Cu_2TC_1 (Fig. 7(a)) distinctly reveals the elemental peaks of Cu 2p, Ti 2p, O 1s, and C 1s at 932.0 eV, 457.5 eV, 530.7 eV, and 283.1 eV, respectively. A least-squares Gaussian fitting model was used for peak deconvolution. Fig. 7(b) depicts the spectra of Ti 2p, where two distinct peaks at 458.6 eV ($2p_{3/2}$) and 464.3 eV ($2p_{1/2}$) indicate the existence of Ti^{4+} oxidation state. The XPS spectrum of C 1s shows two distinct peaks, as shown in Fig. 7(c), a peak at 284.55 eV indicates the presence of SP^2-hybridised carbon atoms, and the other at 288.29 eV indicates the presence of a Ti–O–C bond. This suggests that carbon atoms may have substituted parts of the TiO_2 lattice, creating a Ti–O–C structure during synthesis.[43] The deconvoluted spectrum of O 1 s (Fig. 7(d)) is associated with two peaks of binding energies 529.3 eV and 531.19 eV for Ti–OH and Ti–O bond in lattice oxygen, respectively. The Cu 2p spectrum (Fig. 7(e)) shows peaks at binding energies of 932.04 and 951.81 eV for Cu $2p_{1/2}$ and Cu $2p_{3/2}$, respectively, demonstrating the presence of Cu0 and Cu+.[44] Overall, these findings confirm the successful formation and structural integrity of the Cu_2TC_1 composite.

3.5. Photocatalytic degradation under visible light irradiation

The photocatalytic effectiveness of several synthesized composites was assessed by doxycycline (DOX) photodegradation utilizing a Wipro Garnet B22 50-Watt LED lamp equipped with a wavelength > 360 nm cut-off filter. After 30 minutes in dark conditions, indicating adsorption–desorption equilibrium, around 29% of DOX molecules were adsorbed onto the Cu_2TC_1 composite. In contrast, the adsorption percentages for bare anatase TiO_2, TC_1, A_2T, Cu_2T, and A_2TC_1 samples were 18.3%, 22%, 19.6%, 21.6%, 25.6% respectively. This improved adsorption results from the incorporation of AC, which enlarges the BET surface area and offers numerous sites for DOX adsorption. Once the adsorption–desorption equilibrium was achieved, visible light was used to initiate degradation and further reduce the DOX concentration. Fig. 8(a) illustrates the

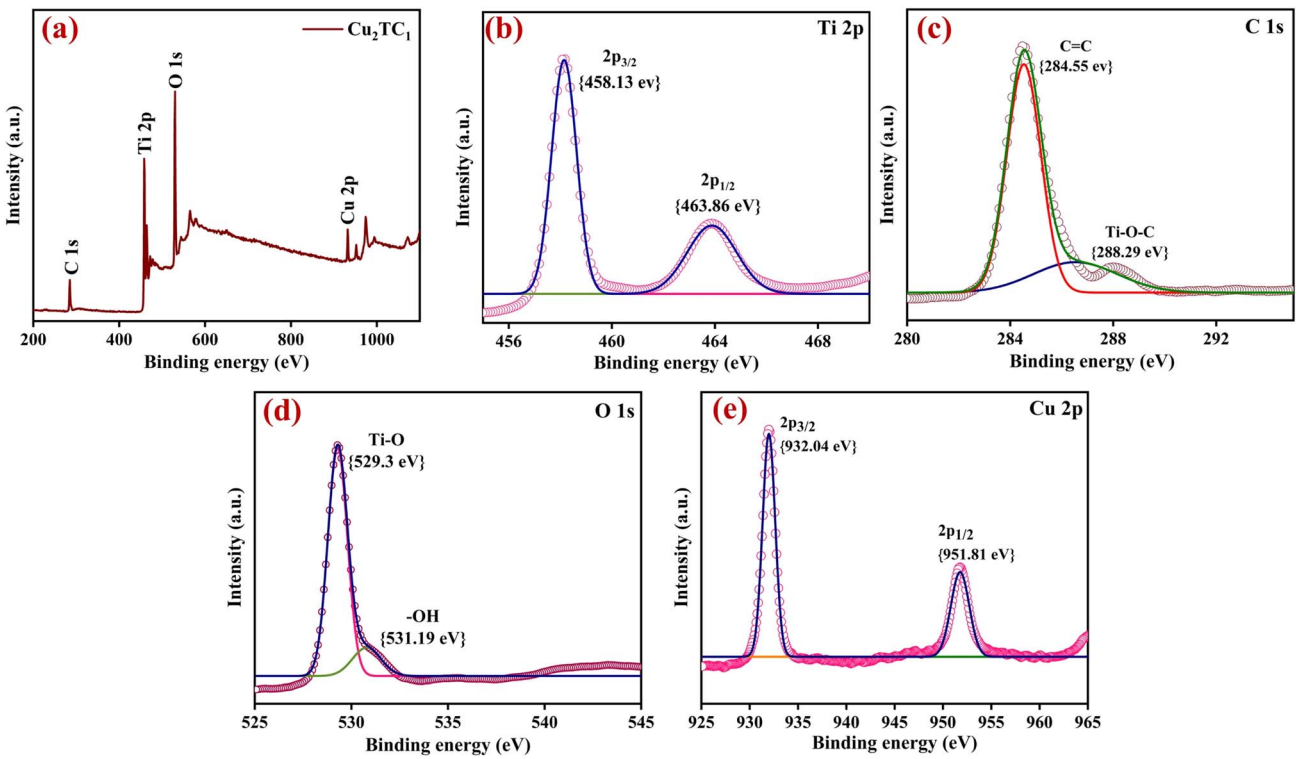

Fig. 7 XPS spectrum of Cu_2TC_1 composite; (a) elemental survey spectrum, (b) Ti 2p, (c) C 1s, (d) O 1s, (e) Cu 2p.

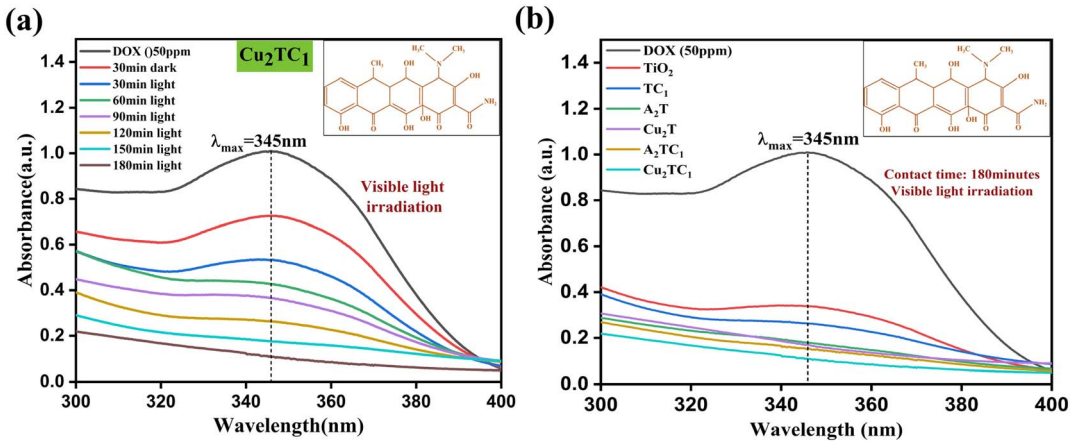

Fig. 8 (a) The decrease in absorbance spectra of doxycycline when exposed to visible light by AC (1 wt%)–Cu (2 wt%)–TiO_2 composite, (b) change in the absorbance spectra of doxycycline by various prepared composites.

change in absorbance of DOX (50 ppm) with Cu_2TC_1 composite under various periods of irradiation (30–180 minutes), exhibiting a maximum absorption peak at 345 nm. When exposed to visible light, the photocatalytic activity of anatase TiO_2 was lower (66.4%) due to its wide band gap (Fig. S6). Following the deposition of 2 wt% Ag and Cu NPs, the composite's band gap decreases, and its degradation efficiency improves, reaching up to 82.1% for A_2T and 83% for Cu_2T. The enhanced activity results from the dual roles of Ag and Cu, the SPR effect improves visible-light absorption, and their function as electron traps promotes efficient charge separation by reducing electron–hole recombination. The Fermi levels of noble metals Ag and Cu are situated near the conduction band of TiO_2.[45,46] This small gap facilitates the transport of photoexcited electrons from the semiconductor surfaces to the Fermi levels of noble metals. This electron-transfer pathway is confirmed by the reduction in photoluminescence intensity and the increased lifetime of the excited species observed in time-resolved PL data for Ag and Cu-modified materials relative to bare materials. Furthermore, Ag and Cu nanoparticles produce active species by converting dissolved O_2 into $^{\bullet}O_2^-$ radicals, which then break down pollutant molecules into simpler forms.[39] Fig. 8(b) illustrates the change in absorption spectra of DOX after 180 minutes of visible light irradiation, indicating that Cu_2TC_1 exhibits the highest degradation of 88.8%, compared to Cu_2T (83%) and TC_1 (75.5%). Copper-modified composites showed enhanced activity than silver-modified composites because Cu (4.93 eV) has a higher work function than Ag (4.2 eV).[47] The effective adsorption of DOX is facilitated by the porous structure of the AC, and the drug's photocatalytic breakdown is supported by the presence of TiO_2. Without photocatalysts, DOX degrades negligibly, indicating that it is highly photostable in visible light. Fig. 9(a and b) shows the concentration profiles (C_t/C_0) over time, illustrating the degradation kinetics under dark and visible light conditions. The comparative histograms, showing the percentage adsorbed (in 30 minutes) and the percentage degraded (in 180 minutes), are given in Fig. 10(a).

To quantitatively examine the kinetics of DOX photocatalytic degradation, a pseudo-first-order rate equation (eqn (4)) was used

$$\ln \frac{C_0}{C_t} = kt \tag{4}$$

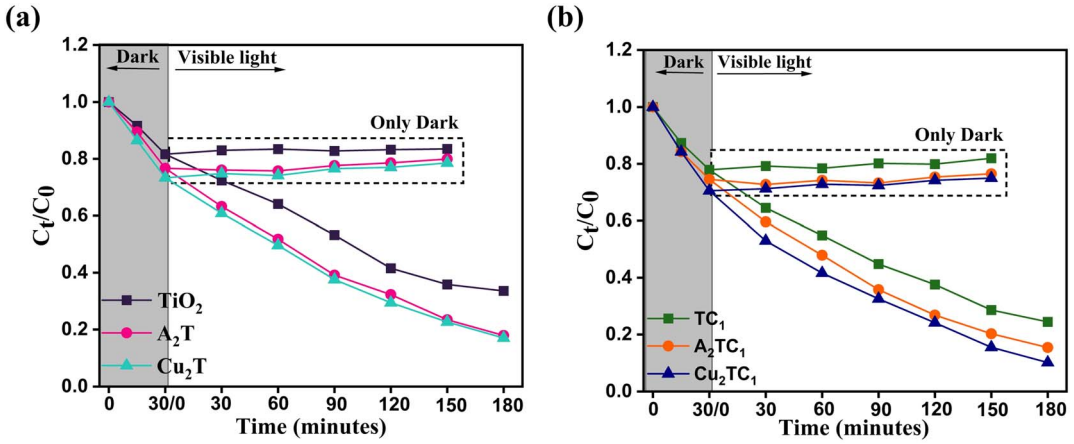

Fig. 9 The time-course degradation efficiency of doxycycline using various composites (a and b) under visible light.

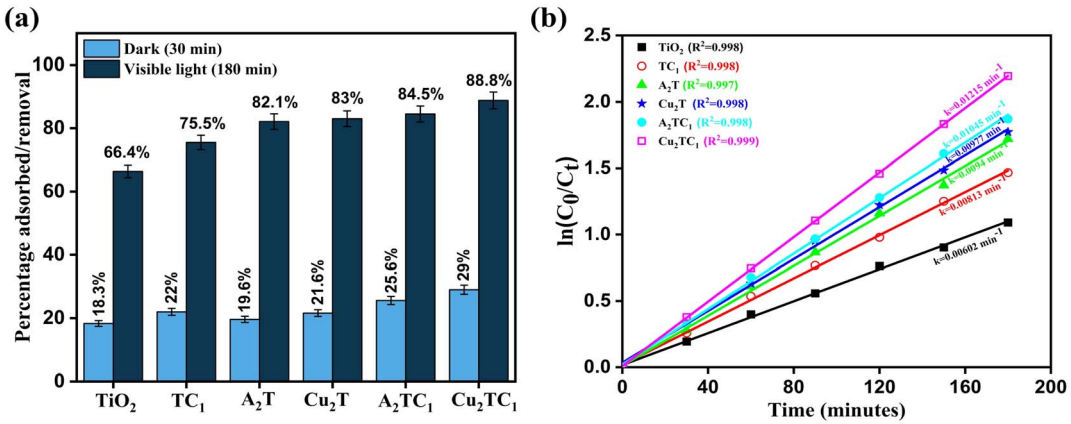

Fig. 10 (a) Percentage adsorbed (under dark) and removal (under visible light) of doxycycline using different catalysts, (b) pseudo-first-order kinetic fitting of degradation efficiencies for various prepared composites under visible light.

where t denotes time, k is the rate constant (in min^{-1}), C_0 and C_t indicate the initial concentration of DOX and concentration at time 't' for all prepared catalysts. For the as-synthesised composites, Fig. 10(b) illustrates the linear relationship between $\ln(C_0/C_t)$ and reaction time. The observed rate constant values for TiO_2, TC_1, A_2T, Cu_2T, A_2TC_1, and Cu_2TC_1 are 0.00602, 0.00813, 0.00094, 0.00977, 0.01045, and 0.01215 min^{-1}, respectively. The highest value of rate constant (k) for Cu_2TC_1 composite aligns with its photodegradation performance (88.8%) and is approximately twice that of bare TiO_2. The photodegradation graphs show that for all materials, the intensity of the DOX absorption maxima (λ_{max} = 345 nm) declines with extended exposure to light. These results highlight the effectiveness of incorporating AC into Ag and Cu–TiO_2 in producing highly efficient photocatalysts.

3.6. Photocatalytic degradation under solar light irradiation

Under natural sunlight, the photocatalytic experiments for the breakdown of the antibiotic DOX using Cu_2TC_1 catalyst was extensively studied. The tests were conducted in June at Patiala, Punjab, where 5 mg of each synthesized catalyst was mixed with 10 mL of a 50 ppm DOX solution and left in the sun for 180 minutes, continuously stirred by a magnetic field. During the procedure, the average solar light intensity was 700 W m^{-2}, and the surrounding temperature remained between 38 °C and 42 °C.

Fig. 11(b) compares the photocatalytic activity of the various composites that were prepared. It reveals that the Cu_2TC_1 composite exhibits the highest degradation efficiency, up to 98.5% after 180 minutes of exposure to solar radiation as compared to bare TiO_2 (68.7%) (Fig. S7). Fig. 11(a) shows the changes in the absorption spectrum of the DOX solution over time using Cu_2TC_1 composite. Because sunlight has a higher photon energy and a wider spectral range than visible light, it has a higher photocatalytic efficiency. Furthermore, compared to exposure to visible light alone, the mild thermal effect of sunlight promotes surface adsorption and reaction kinetics, which together lead to improved photocatalytic performance. The photocatalytic activity of several synthesized composites is arranged as follows: Cu_2TC_1 (98.5%) > A_2TC_1 (92.6%) > Cu_2T

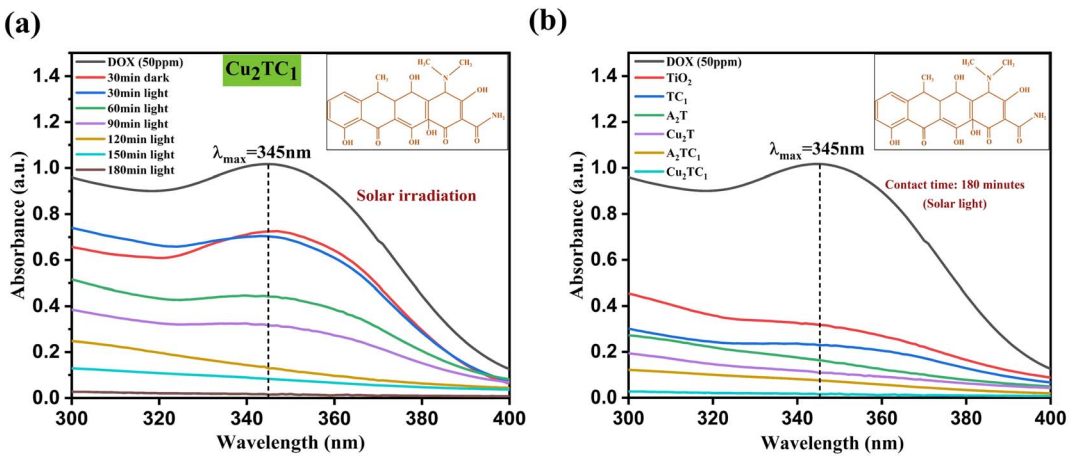

Fig. 11 (a) The decrease in absorbance spectra of doxycycline when exposed to visible light by AC (1 wt%)–Cu (2 wt%)–TiO_2 composite, (b) change in the absorbance spectra of doxycycline by various prepared composites.

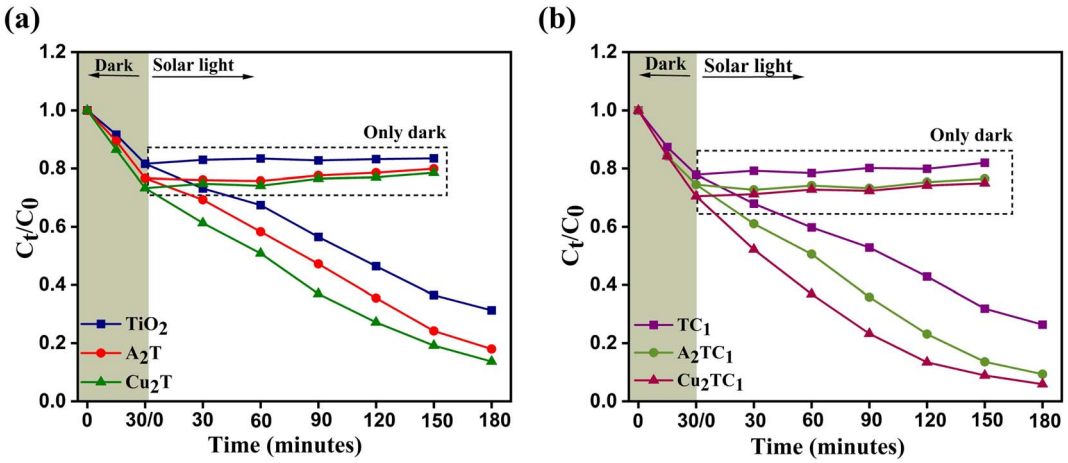

Fig. 12 The time-course degradation efficiency of doxycycline using various composites (a and b) under solar light irradiation.

(89.2%) > A_2T (83.9%) > TC_1 (77.4%) > TiO_2 (68.7%). Fig. 12(a, b) illustrates the degradation kinetics under dark and visible light, displaying the change in concentration profiles (C_t/C_0) of different composites over time. When exposed to solar light, the percentage adsorbed (in 30 minutes) and the percentage degraded (in 180 minutes) are compared in Fig. 13(a).

To provide a quantitative assessment of the DOX degradation kinetics using solar light irradiation, a kinetic plot ($\ln(C_0/C_t)$) as a function of irradiation time was drawn for all the fabricated composites. This plot displays an excellent linear fit (Fig. 13(b)). Among all the fabricated composites, the Cu_2TC_1 composite exhibits the highest rate constant (0.1612 min^{-1}) as compared to Cu_2T (0.01102 min^{-1}), TC_1 (0.00695 min^{-1}), and bare TiO_2 (0.00655 min^{-1}). The pseudo-first-order kinetic constants (k) and associated R^2 values for the modified TiO_2 composites subjected to visible and solar light irradiation are shown in Table 1.

Furthermore, Table 2 compares the degradation efficiency of the Cu_2TC_1 with that of most other photocatalysts for DOX degradation that have been previously reported. The findings suggest that this recently developed photocatalyst is effective in treating wastewater when exposed to visible and solar light.

3.7. Mineralization (TOC removal) of DOX

Mineralizing the targeted organic pollutant is a primary objective of photocatalytic processes. Thus, following treatment with the produced composites, TOC measurement was used to assess the degree of DOX mineralization. To calculate TOC, eqn (5) is applied.

$$\text{Diminerilization efficiency}(\%) = \frac{TOC_0 - TOC}{TOC_0} \quad (5)$$

where TOC_0 and TOC denote the total organic carbon of the starting content and that of the reaction mixture. The amount of mineralization that happens by the conclusion of the procedure is indicated by the decrease in the TOC value. Using Cu_2TC_1, the results demonstrate that after 180 minutes of visible light exposure, the TOC levels of DOX decreased from 16.5 mg L^{-1} to 5.00 mg L^{-1}, which is equivalent to 69.6% of its mineralization, as shown in Fig. 14.

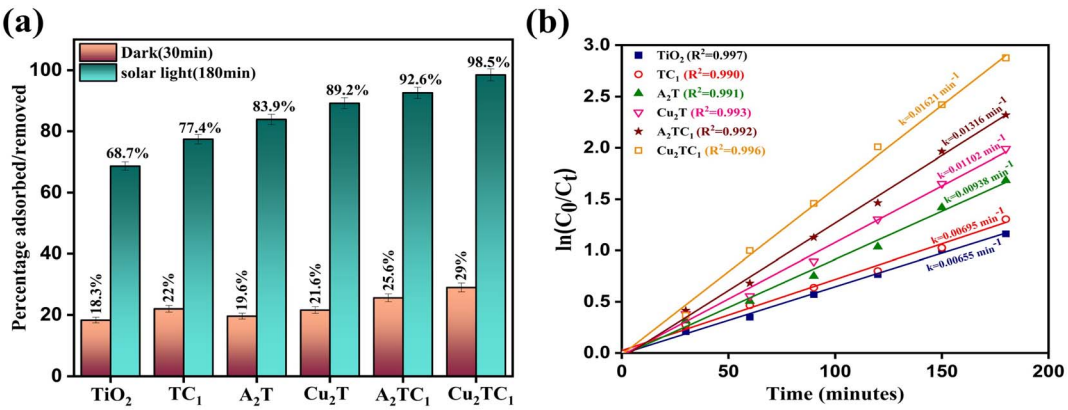

Fig. 13 (a) Percentage adsorbed (under dark) and degradation removal (under solar irradiation) of doxycycline using different catalysts, (b) pseudo-first-order kinetic fitting of various prepared composites under solar light.

Table 1 Kinetic parameters and degradation efficiency of the pseudo-first order model of various composites under visible and solar light irradiation

Pseudo-first-order (visible light)			Pseudo-first-order (solar light)	
Photocatalysts	k (min^{-1}) (R^2)	Degradation efficiency (%)	k (min^{-1}) (R^2)	Degradation efficiency (%)
TiO_2	0.00602 (0.998)	66.4	0.00655 (0.997)	68.7
TC_1	0.00813 (0.998)	75.5	0.00695 (0.990)	77.4
A_2T	0.0094 (0.997)	82.1	0.00938 (0.991)	83.9
Cu_2T	0.00977 (0.998)	83	0.01102 (0.993)	89.2
A_2TC_1	0.01045 (0.998)	84.5	0.01316 (0.992)	92.6
Cu_2TC_1	0.01215 (0.999)	88.8	0.01621 (0.996)	98.5

Table 2 Summary of comparison of different photocatalysts for the degradation of doxycycline

Photocatalyst	DOX conc. (mg L^{-1})	Catalyst dose (g L^{-1})	Light source	Photon flux (W m^{-2})	Irradiation time (minutes)	Rate constant (min^{-1})	Degradation efficiency (%)	Ref.
g-C_3N_4@MIL100	10	1	200 W Xe lamp	—	30	0.0541	82.8	48
TiO_2/g-C_3N_4/biochar	25	0.5	50 W–220 V lamp	—	120	0.0383	91.9	49
CuAl-LDH/CL	40	0.5	50 W LED	~100	120	0.0116	96	5
Ag/AgCl–$CdMoO_4$	—	—	Visible	—	60	0.02114	82.37	12
Al_2O_3–Fe_2O_3–CaO	10	0.3	UV	—	120	0.013	85.1	50
Cu_2TC_1	50	0.5	Sunlight	700	180	0.01621	98.5	This work

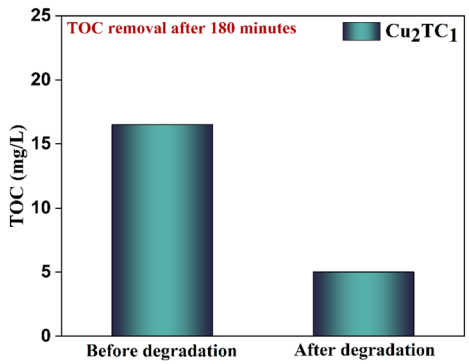

Fig. 14 TOC removal of doxycycline under visible light irradiation.

The results indicate that the composite can mineralize most DOX molecules, which is enough to remove the drug's toxicity and negative ecological impacts. It was also important to observe that the mineralization activity was less than the deteriorating efficiency determined by the absorption spectra. This outcome is typically the consequence of the production of intermediate products. However, complete mineralization of DOX is expected after prolonged exposure to light.

3.8. Detection of active species

We conducted radical trapping studies using scavenger molecules (Fig. 15(a)) to evaluate the role of reactive species in the photodegradation of DOX. The reaction conditions were identical to those previously described, but to scavenge $OH^{\bullet}$, h^+, and $^{\bullet}O_2^-$ radicals, we used IPA, argon gas, and EDTA, respectively. Fig. 15(a) shows that using argon gas followed by EDTA resulted in minimal suppression of photoactivity, suggesting that the $OH^{\bullet}$ radical is the predominant active species responsible for degrading DOX. The trend of the photocatalytic activity obtained by scavenging several active species was as follows: $OH^{\bullet}$ (35%) > $^{\bullet}O_2^-$ (42%) > h^+ (49%). When compared to the decrease brought on by h^+ and $^{\bullet}O_2^-$, it was shown that scavenging $OH^{\bullet}$ radicals decreased the photocatalytic activity by around 53.8%. Therefore, it was inferred that the photodegradation of DOX using the Cu_2TC_1 composite was mainly driven by $OH^{\bullet}$ radicals. When the as-fabricated composites are exposed to visible light, electron–hole pairs (e^-–h^+) are generated. These photoexcited electrons migrate to the Fermi level of Cu and react with O_2 to produce superoxide radicals ($^{\bullet}O_2^-$). Furthermore, some of these radicals interact with water to form hydroxyl radicals ($^{\bullet}OH$), which in turn cause the breakdown of DOX molecules.[51,52]

3.9. Reusability and stability test

The stability and reusability of a photocatalyst are essential for its commercialization and potential uses in industrial processes. To test its recyclability, the most efficient catalyst, Cu_2TC_1, was successfully separated from the degraded solution by centrifugation, thoroughly washed with DI water, dried, and reused for several cycles. When exposed to visible light, the catalyst's photocatalytic efficiency decreases slightly, from 88.8% to 76.5%, after five consecutive trials, indicating that it is very effective at degrading DOX in an aqueous solution (Fig. 15(b)). This 12.3% reduction can be attributed to material losses that occurred during the recovery process.

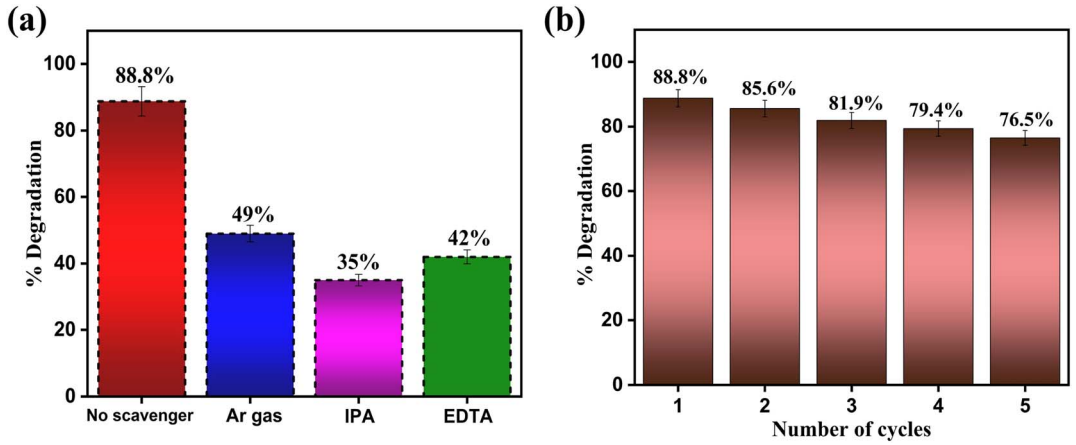

Fig. 15 (a) Effect of various scavengers on the degradation of doxycycline under visible light, (b) the reusability studies of AC (1 wt%)–Cu (2 wt%)–TiO_2 composite.

3.10. Proposed photocatalytic degradation mechanism

Based on the E_g values that were previously computed using DRS, the given equation was utilized to ascertain the locations of the VB and CB potentials at the zero-point charge:

$$E_{VB} = \chi - E^e + 0.5E_g \quad (6)$$

$$E_{CB} = E_{VB} - E_g \quad (7)$$

where E^e is the free electron energy (4.5 eV *vs.* NHE), E_g is the bandgap energy, χ is the photocatalyst's absolute electronegativity (5.90 *vs.* NHE for TiO_2), and valence and conduction band edges are given by E_{VB} and E_{CB}, respectively.

The mechanism shown in Scheme 2 provides a clear explanation for the increased rate of photodegradation. Firstly, DOX molecules get adsorbed on the surface of activated charcoal due to its good pore structures and rich oxygen-containing functional groups. The concentration of pollutants near the TiO_2 increases as a result of AC's capacity to efficiently adsorb pollutants on the surface of the composite material. Upon exposure to light, the electrons in the VB of TiO_2 will acquire photon energy and move into the CB to create photo-generated electrons (e^-). These electrons will then travel to the catalytic surface and be reduced. The photogenerated holes (h^+) formed in the VB undergo oxidation. The VB and CB band edge positions for TiO_2 were determined using eqn (6) and (7), which produced values of +2.89 eV and −0.10 eV, respectively. Since the CB value is less negative than the $E_{O_2}/E_{\cdot O_2^-}$ (−0.046 eV *vs.* NHE) value, it is likely that dissolved O_2 is converted to $^{\cdot}O_2^-$ radicals by electrons in the CB. The holes in the valence band may readily oxidize H_2O to $^{\cdot}OH$ radicals because the E_{VB} value is greater than that of $E_{\cdot OH/H_2O}$ (+2.68 eV *vs.* NHE). These free radicals then cause organic pollutant molecules to break down into smaller molecules.

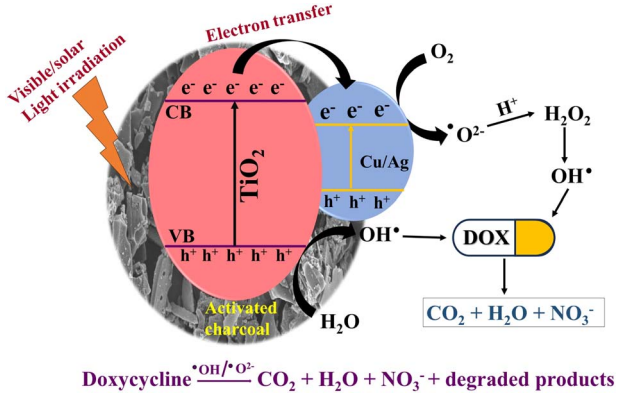

Scheme 2 The schematic reaction mechanism of doxycycline degradation using AC (1 wt%)–Cu (2 wt%)–TiO_2 composite.

Additionally, the SPR effect of Ag and Cu increases the sensitivity of TiO_2 to visible light. When subjected to visible light, the electromagnetic field induces collective oscillations in the conduction band electrons of TiO_2. This process enhances the material's photocatalytic efficiency by promoting the separation of photoinduced electron–hole pairs generated at the TiO_2 surface when exposed to visible light. The DRS and PL findings are in agreement with this. In addition to promoting efficient electron–hole pair separation, AC likely creates a heterojunction with TiO_2, improving TiO_2 dispersion and providing more active sites for photocatalysis. Finally, DOX interacts with the $^{\cdot}OH$ and $^{\cdot}O_2^-$ radical anions to produce H_2O, CO_2, NO_3^-, and other trace organic compounds. The final breakdown products are less likely to adsorb onto AC or TiO_2 due to their lower molecular weight. After that, these materials depart from the photocatalyst surface, creating space for additional DOX molecules to adsorb. The process is crucial for maintaining the effectiveness of photocatalytic reactions and demonstrates the enhanced efficacy of the Cu_2TC_1 composite produced.

3.10.1. Degradation mechanism study using HRMS analysis. The degradation intermediates produced during the photocatalytic degradation of DOX using the Cu_2TC_1 catalyst were analyzed using the HR-MS technique. The goal was to gain a better understanding of the mechanism involved in

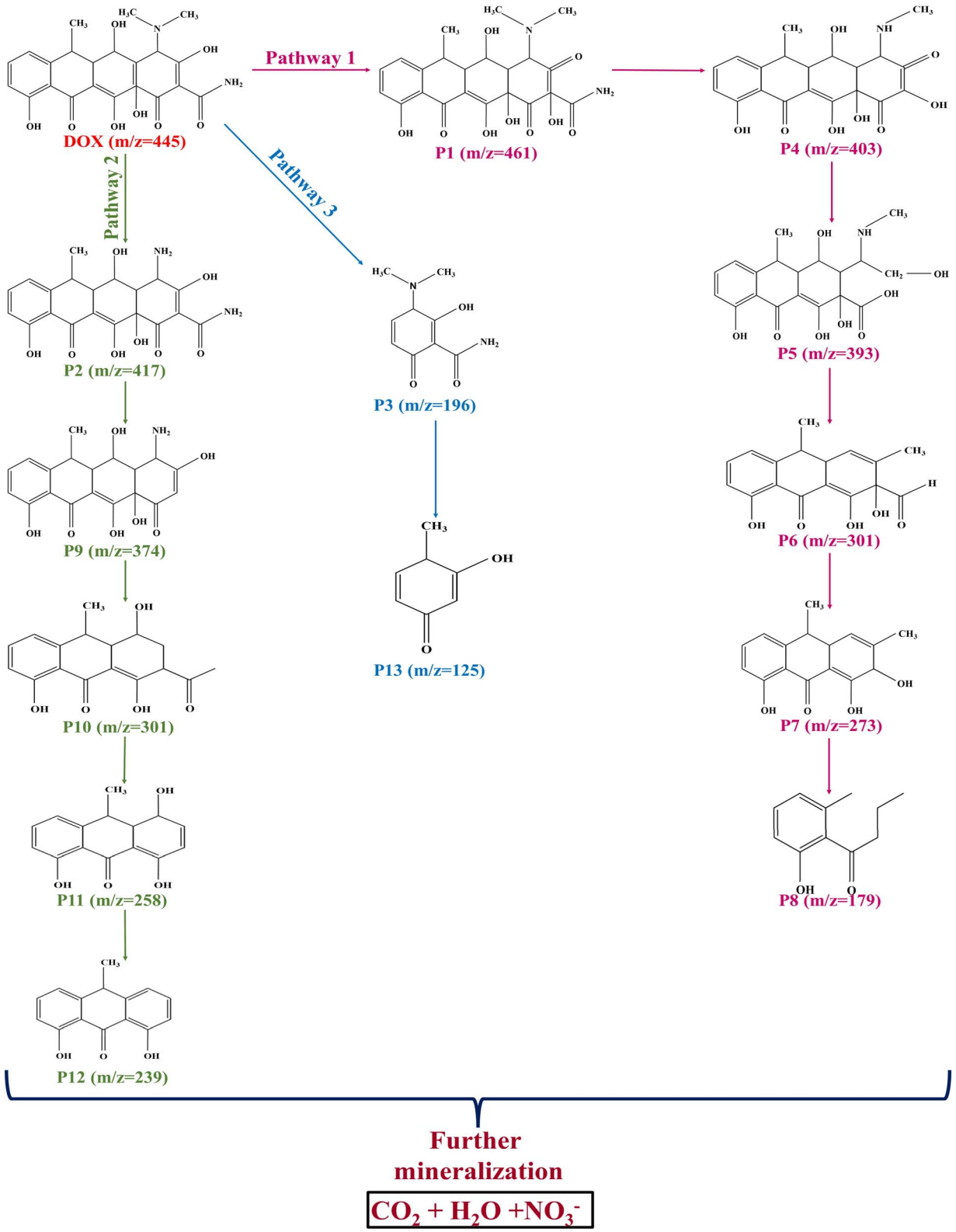

Fig. 16 Proposed degradation route for doxycycline over AC (1 wt%)–Cu (2 wt%)–TiO_2 composite.

doxycycline degradation. For the tests, positive mode electrospray ionization was used. The Cu_2TC_1 catalyst was used to degrade the DOX solution for 180 minutes under exposure to visible light, while following the previously specified photodegradation parameters. To identify the intermediate products formed during the process, the degraded solutions were

collected for analysis after centrifugation. This study will provide insight into the transformation pathways of DOX. Fig. 16 depicts the possible breakdown pathways of DOX using the intermediate products detected in the HR-MS spectra (Fig. S8). Functional group cleavage, ring-opening reactions, and hydroxylation are a few of the ways that DOX interacts with various reactive species. Interestingly, a noticeable peak is observed at $m/z = 445$ for the parent DOX. There are numerous ionizable and electron-rich functional groups in the DOX molecule. They are made up of the conjugated double bond, the dimethylamino group, and the phenolic group. These functional groups are especially susceptible to attack by reactive species like $OH^{\bullet}$, h^{+}, and $^{\bullet}O_2^{-}$.

In Pathway 1, $OH^{\bullet}$ attacked the DOX ($m/z = 445$) molecule, causing it to undergo hydroxylation and become P1 ($m/z = 461$). P4 ($m/z = 403$) was formed as a result of the dimethylamino group being deamidated and demethylated. Ring-opening demethylation of the intermediates occurred as the reaction proceeded, resulting in the formation of simple-structured compounds, namely P5 ($m/z = 393$), P6 ($m/z = 301$), P7 ($m/z = 273$), and P8 ($m/z = 179$).[53,54]

For pathway 2, the demethylation of the DOX results in the formation of P2 ($m/z = 417$). P2 undergoes deamidation to form P9 ($m/z = 374$). The continued action of active species will then result in a ring-opening reaction that produces P10 ($m/z = 301$). P10 eventually changed into P12 ($m/z = 239$) as a result of decarboxylation and elimination of the hydroxyl group.[11]

In pathway 3, DOX ($m/z = 445$) opens its rings to produce P3 ($m/z = 196$). P3 is further demethylated and decarboxylated to produce P13 ($m/z = 125$).[55] All degradation mechanisms ultimately result in organic molecules being transformed into smaller inorganic compounds, such as NO_3^{-}, CO_2, and H_2O. HR-MS analysis revealed that $OH^{\bullet}$, h^{+}, and $^{\bullet}O_2^{-}$ all contributed to the photodegradation of DOX molecules.

4 Conclusion

In conclusion, anatase phase TiO_2 was synthesized *via* a hydrothermal reaction. Further, we synthesized activated charcoal (AC)-modified Ag and Cu–TiO_2 *via* the ultrasonication treatment and the photo-deposition method. With enhanced charge separation and robust optical sensitivity in the visible range, the AC (1 wt%)–Cu (2 wt%)–TiO_2 (Cu_2TC_1) composite has demonstrated itself to be an excellent photocatalyst for DOX degradation. When exposed to sunlight, the photocatalytic response of bare anatase TiO_2 has increased from 68.7% to 98.5% with the incorporation of AC and Cu. The Cu_2TC_1 composite exhibited the highest rate constant values under visible light (0.01215 min^{-1}) and solar light irradiation (0.01621 min^{-1}), in accordance with pseudo-first-order kinetics. The radical trapping experiments and HR-MS data provide a thorough depiction of the reaction mechanism and probable intermediates created during the degradation. The effectiveness of the created photocatalyst in mineralization was also evaluated using a TOC test. The prepared composite displayed excellent stability, with a slight decrease in the activity after five treatment cycles. Overall, the findings suggest that AC (1 wt%)–Cu (2 wt%)–TiO_2 is a cost-effective, efficient, and eco-friendly option for treating pharmaceutical wastewater.

Author contributions

Kirti Bisht: writing the original draft, experimentation, methodology, and data curation. Davinder Kaur: writing – review & editing, validation, supervision, and conceptualization. Bonamali Pal: data validation, supervision, investigation, formal analysis, and conceptualization.

Conflicts of interest

The authors declare that no financial or commercial ties existed that could be interpreted as potential conflicts of interest throughout the research.

Abbreviations

AC	Activated charcoal
SPR	Surface plasmon resonance
NPs	Nanoparticles
wt%	weight%
DOX	Doxycycline
TOC	Total organic carbon
TC_1	AC (1 wt%)–TiO_2
A_2T	Ag (2 wt%)–TiO_2
Cu_2T	Cu (2 wt%)–TiO_2
A_2TC_1	AC (1 wt%)–Ag (2 wt%)–TiO_2
Cu_2TC_1	AC (1 wt%)–Cu(2 wt%)–TiO_2

Data availability

The data supporting the results of this study are available from the corresponding authors upon reasonable request.

Supplementary information (SI) is available. See DOI: https://doi.org/10.1039/d6ra00006a.

Acknowledgements

The authors are thankful to the Department of Physics and Material Science (DPMS) for scanning electron microscopy (SEM) and X-ray diffraction (XRD) measurements, and Sprint testing solutions for HR-TEM analysis. Furthermore, I am grateful for the assistance with total organic carbon (TOC) analysis provided by the Sophisticated Analytical Instrument (SAI) Labs at Thapar Institute of Engineering and Technology (TIET). The authors are also grateful to DST-FIST for their assistance with HRMS analysis.

References

1 Q. Zhang, G. Ying, C. Pan, Y. Liu and J. Zhao, *Environ. Sci. Technol.*, 2015, **49**, 6772–6782, DOI: 10.1021/acs.est.5b00729.
2 M. Qiao, G. Ying, A. C. Singer and Y. Zhu, *Environ. Int.*, 2018, **110**, 160–172, DOI: 10.1016/j.envint.2017.10.016.

3 H. Kim, I. Lee and J. Oh, *Sci. Total Environ.*, 2017, **579**, 940–949, DOI: 10.1016/j.scitotenv.2016.10.039.
4 N. Van Hung, B. T. Nguyet, N. H. Nghi, N. M. Luon, N. N. Bich, L. V. Son, N. T. Kien, D. N. Nhiem, N. T. Tuoi and D. Q. Khieu, *Environ. Eng. Res.*, 2024, **29**, 230596, DOI: 10.4491/eer.2023.596.
5 M. Bansal and B. Pal, *Int. J. Biol. Macromol.*, 2025, **285**, 138329, DOI: 10.1016/j.ijbiomac.2024.138329.
6 M. Spina-Cruz, M. G. Maniero and J. R. Guimarães, *Environ. Sci. Pollut. Res.*, 2019, **26**, 27604–27619, DOI: 10.1007/s11356-018-2149-1.
7 S. Zaidi, T. Chaabane, V. Sivasankar, A. Darchen, R. Maachi, T. A. M. Msagati and M. Prabhakaran, *Process Saf. Environ. Prot.*, 2016, **102**, 450–461, DOI: 10.1016/j.psep.2016.04.013.
8 S. Zaidi, V. Sivasankar, T. Chaabane, V. Alonzo, K. Omine, R. Maachi, A. Darchen and M. Prabhakaran, *J. Environ. Chem. Eng.*, 2019, **7**, 102876, DOI: 10.1016/j.jece.2018.102876.
9 Y. Kong, L. Wang, Y. Ge, H. Su and Z. Li, *J. Hazard. Mater.*, 2019, **368**, 33–41, DOI: 10.1016/j.jhazmat.2019.01.026.
10 H. Djelal, P. E. Martinez, D. Haddouche and M. Chabani, *Ecocycles*, 2020, **6**, 25–31, DOI: 10.19040/ecocycles.v6i2.175.
11 J. Bolobajev, M. Trapido and A. Goi, *Chemosphere*, 2016, **153**, 220–226, DOI: 10.1016/j.chemosphere.2016.03.042.
12 X. J. Wen, C. H. Shen, C. G. Niu, D. C. Lai, M. S. Zhu, J. Sun, Y. Hu and Z. H. Fei, *J. Mol. Liq.*, 2019, **288**, 111063, DOI: 10.1016/j.molliq.2019.111063.
13 Ur R. Zia, U. Shah, A. Alam, Z. Shah, K. Shaheen, S. B. Khan and S. Ali Khan, *Inorg. Chem. Commun.*, 2023, **148**, 110312, DOI: 10.1016/j.inoche.2022.110312.
14 K. Anwar, F. K. Naqvi, S. Beg and S. Haneef, *J. Mol. Struct.*, 2023, **1272**, 134183, DOI: 10.1016/j.molstruc.2022.134183.
15 L. Xu, X. Bai, L. Guo, S. Yang, P. Jin and L. Yang, *Chem. Eng. J.*, 2019, **357**, 473–486, DOI: 10.1016/j.cej.2018.09.172.
16 S. Panwar, G. K. Upadhyay and L. P. Purohit, *Mater. Res. Bull.*, 2022, **145**, 111534, DOI: 10.1016/j.materresbull.2021.111534.
17 F. Afriani, Y. Tiandho, D. A. Hapidin, F. M. Dwivany and K. Khairurrijal, *Comput. Mater. Sci.*, 2023, **230**, 112462, DOI: 10.1016/j.commatsci.2023.112462.
18 R. Sharma, S. Barman and B. Pal, *Microporous Mesoporous Mater.*, 2026, **400**, 113892, DOI: 10.1016/j.micromeso.2025.113892.
19 M. Mahanti and D. Basak, *Chem. Phys. Lett.*, 2014, **612**, 101–105, DOI: 10.1016/j.cplett.2014.08.002.
20 A. Alam, W. U. Rahman, Z. U. Rahman, S. A. Khan, Z. Shah, K. Shaheen, H. Suo, M. N. Qureshi, S. B. Khan, E. M. Bakhsh and K. Akhtar, *J. Mater. Sci.: Mater. Electron.*, 2022, **33**, 4255–4267, DOI: 10.1007/s10854-021-07619-2.
21 X. C. Ma, Y. Dai, L. Yu and B. B. Huang, *Light Sci. Appl.*, 2016, **5**, e16017, DOI: 10.1038/lsa.2016.17.
22 S. Yang, L. Wang, Y. Yan, L. Yang, X. Li, Z. Lu, H. Zhai, D. Han and P. Huo, *Sci. Rep.*, 2019, **9**, 16863, DOI: 10.1038/s41598-019-53212-3.
23 C. Qin, H. Wang, X. Yuan, T. Xiong, J. Zhang and J. Zhang, *Chem. Eng. J.*, 2020, **382**, 122977, DOI: 10.1016/j.cej.2019.122977.
24 D. Kaur, K. Singh, W. T. Reynolds and B. Pal, *Environ. Sci. Pollut. Res.*, 2023, **30**, 97660–97672, DOI: 10.1007/s11356-023-29301-2.
25 T. S. Jamil, M. Y. Ghaly, N. A. Fathy, T. A. Abd El-Halim and L. Österlund, *Sep. Purif. Technol.*, 2012, **98**, 270–279, DOI: 10.1016/j.seppur.2012.06.018.
26 D. C. Gloria, C. H. Brito, T. A. Mendonça, T. R. Brazil, R. A. Domingues, N. C. Vieira, E. B. Santos and M. Gonçalves, *Mater. Chem. Phys.*, 2023, **305**, 127947, DOI: 10.1016/j.matchemphys.2023.127947.
27 R. Girija, S. Mary, G. Balakrishnan, S. M. Mariappan, M. S. Hamdy and M. Shkir, *ChemistrySelect*, 2022, **7**, e202103614, DOI: 10.1002/slct.202103614.
28 M. Baruah, S. L. Ezung, S. Sharma, U. B. Sinha and D. Sinha, *Inorg. Chem. Commun.*, 2022, **144**, 109905, DOI: 10.1016/j.inoche.2022.109905.
29 N. A. Yaacob, A. Khasri, N. H. Mohd Salleh and M. R. Mohd Jamir, *J. Dispersion Sci. Technol.*, 2024, **45**, 249–260, DOI: 10.1080/01932691.2022.2143367.
30 M. Baruah, S. L. Ezung, A. Supong, P. C. Bhomick, S. Kumar and D. Sinha, *Korean J. Chem. Eng.*, 2021, **38**, 1277–1290, DOI: 10.1007/s11814-021-0830-4.
31 K. Santhi, M. Navaneethan, S. Harish, S. Ponnusamy and C. Muthamizhchelvan, *Appl. Surf. Sci.*, 2020, **500**, 144058, DOI: 10.1016/j.apsusc.2019.144058.
32 M. Deng, H. Yang, L. Peng, L. Zhang, L. Tan, G. He, M. Shao, L. Li and Z. Wei, *J. Energy Chem.*, 2022, **74**, 111–120, DOI: 10.1016/j.jechem.2022.06.047.
33 K. Santhi, M. Navaneethan, S. Harish, S. Ponnusamy and C. Muthamizhchelvan, *Appl. Surf. Sci.*, 2020, **500**, 144058, DOI: 10.1016/j.apsusc.2019.144058.
34 S. Janitabar Darzi, A. R. Mahjoub and A. Bayat, *Int. J. Nano Dimens.*, 2016, **7**, 33–40, DOI: 10.7508/ijnd.2016.01.004.
35 M. Kaur, P. Hait and S. Basu, *RSC Adv.*, 2025, **15**, 37166–37182, DOI: 10.1039/d5ra06146f.
36 K. Y. Foo and B. H. Hameed, *Adv. Colloid Interface Sci.*, 2010, **159**, 130–143, DOI: 10.1016/j.cis.2010.06.002.
37 S. S. Jemini and B. Pal, *Appl. Clay Sci.*, 2024, **250**, 107281, DOI: 10.1016/j.clay.2024.107281.
38 Y. Liang, N. Guo, L. Li, R. Li, G. Ji and S. Gan, *New J. Chem.*, 2016, **40**, 1587–1594, DOI: 10.1039/c5nj02388b.
39 S. Kaur and B. Pal, *J. Water Process Eng.*, 2024, **58**, 104765, DOI: 10.1016/j.jwpe.2023.104765.
40 G. A. Crosby and J. N. Demas, *J. Phys. Chem.*, 1971, **75**, 991–1024, DOI: 10.1021/j100678a001.
41 S. Liu, L. Han, Y. Duan, S. Asahina, O. Terasaki, Y. Cao, B. Liu, L. Ma, J. Zhang and S. Che, *Nat. Commun.*, 2012, **3**, 1216, DOI: 10.1038/ncomms2215.
42 T. Umebayashi, T. Yamaki, H. Itoh and K. Asai, *J. Phys. Chem. Solids*, 2002, **63**, 1909–1920, DOI: 10.1016/S0022-3697(02)00177-4.
43 S. Kochar and B. Pal, *Biomass Bioenergy*, 2026, **204**, 108441, DOI: 10.1016/j.biombioe.2025.108441.
44 S. Chen, X. Li, W. Zhou, S. Zhang and Y. Fang, *Appl. Surf. Sci.*, 2019, **466**, 254–261, DOI: 10.1016/j.apsusc.2018.10.036.

45 P. Nayak, S. Kumar, I. Sinha and K. K. Singh, *Environ. Sci. Pollut. Res.*, 2019, **26**, 16279–16288, DOI: 10.1007/s11356-019-04986-6.
46 S. Ghosh, V. S. Goudar, K. G. Padmalekha, S. V. Bhat, S. S. Indi and H. N. Vasan, *RSC Adv.*, 2012, **2**, 930–940, DOI: 10.1039/c1ra00815c.
47 P. Sangpour, F. Hashemi and A. Z. Moshfegh, *J. Phys. Chem. C*, 2010, **114**, 13955–13961, DOI: 10.1021/jp910454r.
48 W. Liu, Q. Kang, L. Wang, L. Wen and Z. Li, *Colloids Surf., A*, 2022, **635**, 128057, DOI: 10.1016/j.colsurfa.2021.128057.
49 S. H. Nguyen, M. T. Tran, P. D. Fisher, J. Clemens, J. Z. Hilt, Y. Tong, J. Kang, Z. Chen, N. V. Hung, B. T. M. Nguyet, N. N. Bich, N. M. Luon, N. N. Dao, N. T. Kien, V. T. S. Le, N. T. Tuoi and D. Q. Khieu, *Mater. Res. Express*, 2024, **11**, 055601, DOI: 10.1088/2053-1591/ad4776.
50 B. A. Ajayi, A. Bamisaye, N. O. Etafo, K. A. Adegoke, Y. A. Alli, A. E. Bukola and M. A. Idowu, *Nano-Struct. Nano-Objects*, 2025, **43**, 101536, DOI: 10.1016/j.nanoso.2025.101536.
51 C. Zhang, Z. Zheng, Z. Wang, F. Deng, X. Li and J. Zou, *Chem. Eng. J.*, 2025, **504**, 158286, DOI: 10.1016/j.cej.2024.158286.
52 C. Xu, X. Liu, Y. Zhang, F. Liao, S. Hu, A. Munnir, R. Su and F. Deng, *J. Environ. Chem. Eng.*, 2025, **13**, 115957, DOI: 10.1016/j.jece.2025.115957.
53 P. Hong, Y. Li, J. He, A. Saeed, K. Zhang, C. Wang, L. Kong and J. Liu, *Appl. Surf. Sci.*, 2020, **526**, 146557, DOI: 10.1016/j.apsusc.2020.146557.
54 H. Xu, K. Zhu, N. S. Alharbi, S. O. Rabah and C. Chen, *Chemosphere*, 2023, **333**, 138917, DOI: 10.1016/j.chemosphere.2023.138917.
55 Z. Deng, X. Zheng and Y. Guo, *Appl. Surf. Sci.*, 2023, **641**, 158407, DOI: 10.1016/j.apsusc.2023.158407.